Acta Materialia 141 (2017) 59–66

Contents lists available at ScienceDirect

Acta Materialia

journal homepage: www.elsevier.com/locate/actamat

Full length article

Microstructural origins of high strength and high ductility in an $AlCoCrFeNi_{2.1}$ eutectic high-entropy alloy

Xuzhou Gao [a, 1], Yiping Lu [b, 1], Bo Zhang [c], Ningning Liang [a], Guanzhong Wu [a], Gang Sha [c], Jizi Liu [c], Yonghao Zhao [a, *]

[a] Nano Structural Materials Center, School of Materials Science and Engineering, Nanjing University of Science and Technology, Nanjing, 210094, China
[b] Key Laboratory of Solidification Control and Digital Preparation Technology (Liaoning Province), School of Materials Science and Engineering, Dalian University of Technology, Dalian, 116024, China
[c] Herbert Gleiter Institute of Nanoscience, Nanjing University of Science and Technology, Nanjing, 210094, China

ARTICLE INFO

Article history:
Received 13 January 2017
Received in revised form
17 July 2017
Accepted 18 July 2017
Available online 24 July 2017

Keywords:
Dislocation planar slip
Eutectic high-entropy alloys
Microstructures
Precipitation-strengthening
Stacking faults
Strength and ductility

ABSTRACT

Recent studies indicate that eutectic high-entropy alloys can simultaneously possess high strength and high ductility, which have potential applications in industrial fields. Nevertheless, microstructural origins of the excellent strength–ductility combination remain unclear. In this study, an $AlCoCrFeNi_{2.1}$ eutectic high-entropy alloy was prepared with face-centered cubic (FCC)($L1_2$)/body-centered-cubic (BCC)(B2) modulated lamellar structures and a remarkable combination of ultimate tensile strength (1351 MPa) and ductility (15.4%) using the classical casting technique. Post-deformation transmission electron microscopy revealed that the FCC($L1_2$) phase was deformed in a matter of planar dislocation slip, with a slip system of {111} <110>, and stacking faults due to low stacking fault energy. Due to extreme solute drag, high densities of dislocations are distributed homogeneously at {111} slip plane. In the BCC(B2) phase, some dislocations exist on two {110} slip bands. The atom probe tomography analysis revealed a high density of Cr-enriched nano-precipitates, which strengthened the BCC(B2) phase by Orowan mechanisms. Fracture surface observation revealed a ductile fracture in the FCC($L1_2$) phase and a brittle-like fracture in the BCC(B2) lamella. The underlying mechanism for the high strength and high ductility of $AlCoCrFeNi_{2.1}$ eutectic high-entropy alloy was finally analyzed based on the coupling between the ductile FCC($L1_2$) and brittle BCC(B2) phases.

1. Introduction

High-entropy alloys (HEAs), which emerged in 2004, are solid solution multicomponent alloys that contain more than four principal elements in equal or non-equal atomic percentage [1–5]. HEAs are a new kind of alloys because they are different from conventional alloys that have one or two principal elements as main components. HEAs have attracted increasing attention recently due to their unique atomic structure and properties, such as high strength of body-centered-cubic (BCC) AlCoCrFeNi alloy at room temperature and TaNbHfZrTi alloy at elevated temperatures, high ductility of face-centered cubic (FCC) CrMnFeCoNi alloy and transformation-induced plasticity-assisted meta-stable dual-phase $Fe_{50}Mn_{30}Co_{10}Cr_{10}$ alloy, sluggish diffusion, and high thermal stability [6–17].

The review of literature indicates that two kinds of HEAs have been widely investigated in the last 10 years: single-phase FCC HEAs and BCC HEAs. Single-phase FCC HEAs generally have high tensile ductility but low yield strength. Examples are CrMnFeCoNi alloy with an elongation to failure of ~50% and yield strength of ~410 MPa [7], $Fe_{40}Mn_{40}Co_{10}Cr_{10}$ alloy with a tensile ductility of ~58% and low yield strength of ~240 MPa [17], and $Fe_{40}Mn_{26}Ni_{27}Co_5Cr_2$ alloy with a total elongation to failure of ~58% and low yield strength of ~95 MPa at room temperature [18]. However, BCC HEAs have high yield strength but low ductility. For example, [316]-oriented and [001]-oriented $Nb_{25}Mo_{25}Ta_{25}W_{25}$ single crystalline pillars have an extraordinarily high strength level (about 4–4.5 GPa) but low plasticity (less than 0.2%) [19]. Therefore, for the single-phase HEAs, it seems difficult to achieve a balance between high strength and high ductility. In addition, the industrial applications of HEAs are restricted certainly by poor castability,

* Corresponding author.
E-mail address: yhzhao@njust.edu.cn (Y. Zhao).
[1] These authors contributed equally to this work.

http://dx.doi.org/10.1016/j.actamat.2017.07.041

liquidity, and composition segregation.

Recently Lu et al. [20] proposed a designation concept of eutectic high-entropy alloys (EHEAs) to combine the high strength of BCC HEAs and high ductility of FCC HEAs and produced an $AlCoCrFeNi_{2.1}$ EHEA with regular FCC($L1_2$)/BCC(B2) lamellar structures and an excellent combination of high strength and high ductility. More recently, the mechanical properties of $AlCoCrFeNi_{2.1}$ EHEA were optimized by thermal mechanical processes, that is, multi-pass cold rolling to a 90% reduction in thickness and subsequently annealed at 800–1200 °C for 1 h [21,22]. As a result, the processed HEAs had tensile ductility more than 10% and high tensile strength greater than 1 GPa. This indicated that the properties of the EHEA could be successfully tailored using thermo-mechanical processing for a wide range of engineering applications. However, the microstructural origins of excellent strength–ductility combination and underlying deformation mechanisms of EHEAs still need systematic investigations.

In this study, transmission electron microscopy (TEM) and atom probe tomography (APT) were used to systematically characterize the microstructural characteristics of post-deformed $AlCoCrFeNi_{2.1}$ EHEA to find answers to the aforementioned problems.

2. Experiments

The master alloy of the eutectic $AlCoCrFeNi_{2.1}$ (elements in atomic ratios) was prepared from commercially pure elements (99.9 wt% for Al, Co, and Ni; 99.5–99.6 wt.% for Cr and Fe) in a ZrO_2 crucible of a vacuum induction melting furnace. The ZrO_2 crucible was first heated to 600 °C and held for 1 h to remove the water vapor. After the elements (approximately 2.5 kg) were put into the furnace, the furnace chamber was evacuated to 0.06 Pa and back-filled with high-purity argon gas to reach 0.06 MPa. The elements were finally melted, superheated, and poured into a high-purity graphite crucible with an inner length of 220 mm, upper inner diameter of 62 mm, and bottom inner diameter of 50 mm. The pouring temperature was set to be 1500 °C. A TRTM-2CK infrared pyrometer was used to monitor the temperature with an absolute accuracy of ± 2 °C. A Walter + bai LFM 20 kN tensile testing machine was used for tensile testing at room temperature with a normal strain rate of 1×10^{-3} s^{-1}. The flat dog bone-shaped tensile samples had a gauge dimension of $20 \times 3 \times 2$ mm^3. The strain was measured using a standard non-contacting video extensometer. Three tensile specimens were measured to obtain reliable results.

Microstructure and composition analyses were carried out by means of x-ray diffraction (XRD), electron back-scattered diffraction (EBSD), TEM, and APT. Specifically, the XRD analyses of crystalline structures were performed on a Bruker D8 with Cu radiation target scanning 2θ from 20 to 80°. EBSD of as-cast specimen was conducted using a high-resolution field emission Carl Zeiss-Auriga-45-66 scanning electron microscope (SEM) equipped with a fully automatic Oxford Instruments Aztec 2.0 EBSD system (channel 5 software). Before EBSD, the specimens were mechanically polished and then electro-polished in an electrolyte containing 90 vol.% acetic acid and 10 vol.% perchloric acid using a voltage of 50 V and polishing time of 45 s in Buehler electromet-4. TEM observations were conducted in a FEI-Tecnai G^2 20 S-TWIN microscope operated at 200 kV, and the high-resolution TEM (HRTEM) was conducted on a Titan G2 60-300. TEM specimens were prepared as follows: the tensile deformed gauge parts were carefully ground to foils with a thickness of about 50 μm, punched into disks with a diameter of 3 mm, and finally electro-polished to an electron-transparent thickness in an aqueous electrolyte containing 10% perchloric acid and 90% ethanol at −25 °C using a twin-jet polishing system. The HRTEM specimen was prepared by means of ion milling on a GATAN 691 to avoid the different electro-polishing rates of the two eutectic phases.

The APT specimen was prepared by electro-polishing combined with a focus iron beam (FIB) cutting along the phase interface. A low-energy (5 keV) Ga beam was used for final ion milling to minimize beam damage. The APT experiment was performed with a local electrode atom probe (LEAP 4000X Si) under ultraviolet laser pulsing at a laser energy of 40 pJ, a pulse repetition rate of 200 kHz, and a target evaporation rate of 0.5% per pulse at 25 K. APT data reconstruction and quantitative analysis were performed using a CAMECA visualization and analysis software (IVAS) 3.6.8.

3. Results

3.1. Initial structures and tensile testing results

Fig. 1a shows the XRD pattern of the as-cast $AlCoCrFeNi_{2.1}$ alloy. The as-cast $AlCoCrFeNi_{2.1}$ alloy consisted of FCC($L1_2$) and BCC(B2) dual-phase. The $L1_2$ and B2 structures, which were further confirmed by subsequent TEM-SAEDs (select area electron-beam diffraction patterns), were consistent with the results reported in the literature [21,22]. Fig. 1b shows the large-area EBSD phase mapping of typical FCC($L1_2$)/BCC(B2) lamellar microstructures. Fine BCC(B2) lamellae (about 2 μm thick, yellow color) were parallel to each other and distributed in the FCC($L1_2$) phase (cyan color). In addition, some coarse BCC(B2) lamellae and islands also appeared. The volume fraction of FCC($L1_2$) and BCC(B2) phases was about 66.3% and 31.2%, respectively. Moreover, some amounts of high-angle grain boundaries (marked in red) were formed during casting.

Tensile testing showed that the as-cast $AlCoCrFeNi_{2.1}$ alloy possessed an excellent combination of high strength and high ductility owing to the uniform FCC($L1_2$)/BCC(B2) lamellar microstructures. Fig. 2 shows the tensile engineering and true stress–-strain curves of the as-cast $AlCoCrFeNi_{2.1}$ alloy. It is evident that the ultimate tensile stress was 1100 ± 50 MPa and the ductility was 18 ± 2%. When the engineering stress–strain curve (blue line) was converted into a true stress–strain curve (red line), the ultimate tensile stress and ductility were 1351 MPa and 15.4%, respectively.

3.2. Deformation mechanisms via TEM characterizations

3.2.1. Deformation of FCC($L1_2$) phase

TEM observations were performed to reveal the deformation mechanisms and understand the mechanical properties. Fig. 3a shows a representative bright-field TEM micrograph of the tensile tested $AlCoCrFeNi_{2.1}$ EHEA. Distinct modulated FCC($L1_2$) and BCC(B2) lamellar structures were obviously observed based on different contrasts (bright and dark, respectively) in the TEM image. This was because the FCC($L1_2$) phase was thinner than the BCC(B2) phase after twin-jet polishing. This chemical polishing result also suggested that the corrosion resistance of BCC(B2) phase was better than that of FCC($L1_2$) phase. Fig. 3b and c show the TEM-SAEDs of FCC($L1_2$) and BCC(B2) phases, respectively. The presence of superlattice spots obtained from the two phases (marked by cyan and yellow circles, respectively) revealed both ordered $L1_2$ (Fig. 3b) and B2 (Fig. 3c) phases. The formation of ordered $L1_2$ structure is rarely reported in eutectic alloys in the literature, whereas the formation of ordered B2 phase is frequently reported owing to the strong negative enthalpy in the Al–Ni system [23–25]. The compositions of the present B2 phase were revealed as ~38 at.% Ni and ~37 at.% Al by the following APT analysis (see Table 1), which hinted that Ni and Al atoms alternately occupied the lattice sites in the B2 unit cell, and other element atoms were substitutional solution atoms [26–28].

The deformation mechanisms of FCC($L1_2$) and BCC(B2) phases

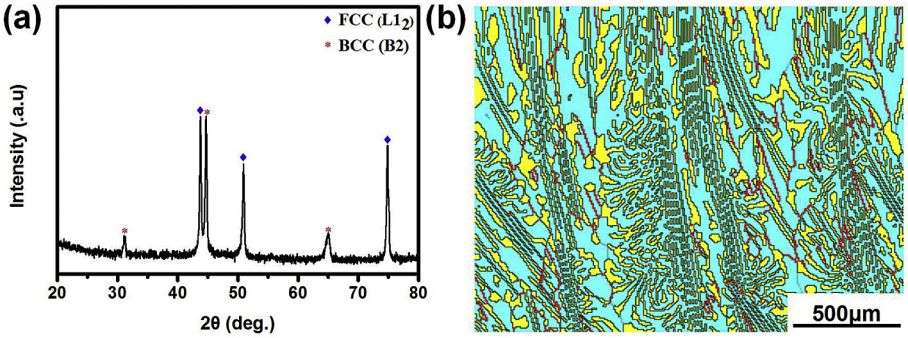

Fig. 1. (a) XRD pattern and (b) EBSD mapping of AlCoCrFeNi$_{2.1}$ alloy. The FCC(L1$_2$) and BCC(B2) phases, phase boundaries and high-angle grain boundaries are marked in cyan, yellow, black and red colors, respectively. (For interpretation of the references to colour in this figure legend, the reader is referred to the web version of this article.)

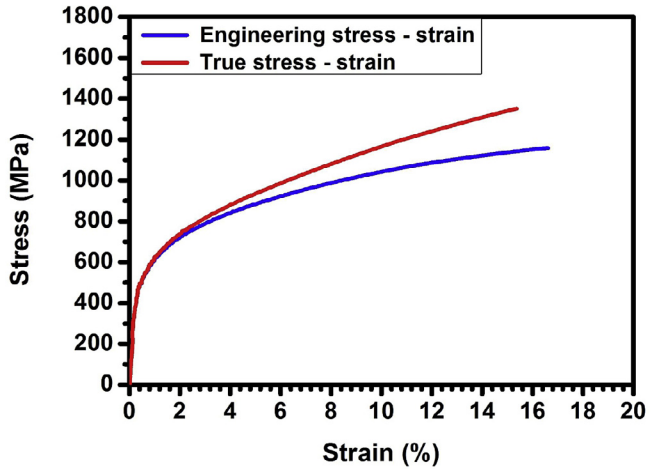

Fig. 2. Tensile stress-strain curves of the AlCoCrFeNi$_{2.1}$ alloy.

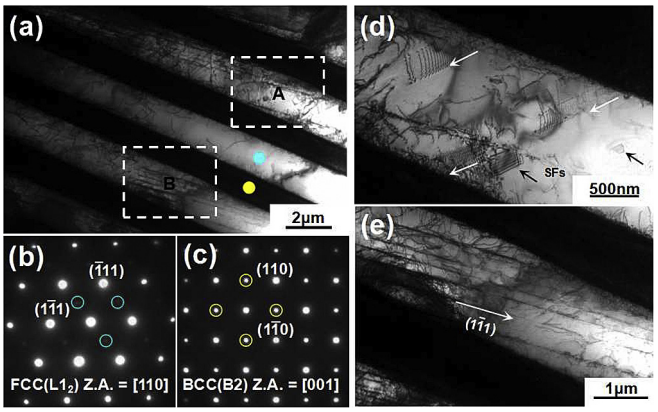

Fig. 3. (a) Bright-field image of the tensile tested FCC(L1$_2$)/BCC(B2) lamellar structure with zone axis of [110] for FCC(L1$_2$) and [001] for BCC(B2); (b) and (c) the SAEDs corresponding to the L1$_2$ and B2 phases, respectively. Super-lattice diffraction spots are indicated by cyan and yellow circles, respectively; (d) magnified image of region "A" in (a) showing the parallel dislocation arrays and SFs; (e) magnified image of region "B" in (a) showing (111) slip traces. (For interpretation of the references to colour in this figure legend, the reader is referred to the web version of this article.)

were different from each other. Fig. 3d is a magnified TEM image of FCC(L1$_2$) phase region marked "A" in Fig. 3a. Several arrays of parallel mobile dislocations could be discerned, as pointed by the white arrows. The specimen tilting technique [29] was used to determine the slip plane of parallel dislocations, and as a result, the dislocation glide was clearly localized on a distinct set of {111} type FCC lattice planes. From the density of parallel dislocations in the array, one could judge that the dislocations were emitted from the FCC(L1$_2$)/BCC(B2) phase boundaries. Besides high-density parallel dislocations in the FCC(L1$_2$) phases, the presence of some stacking faults (SFs, marked by black arrows in Fig. 3d) was worth noting. Fig. 3e is a magnified TEM image of FCC(L1$_2$) phase region "B" in Fig. 3a. One can observe some $(\bar{1}\ 11)$ slip traces through the FCC(L1$_2$) lamella. The distance between the slip traces was about 250 nm. In addition, two kinds of {111} slip traces were also observed to intersect with each other (Fig. 4b).

The parallel unit dislocations, partial dislocations (SF$_S$), and long straight (111) slip traces indicated that the dislocations glided in a manner of planar slip in the FCC(L1$_2$) phase. The slip traces running through the FCC(L1$_2$) lamella revealed that massive dislocations could be motivated on an FCC(L1$_2$)/BCC(B2) phase boundary and slipped on their initial slip planes to the opposite side of the phase boundary without cross-slip. The planar slip nature of the FCC(L1$_2$) phase resulted from the low stacking fault energy (SFE), which was further evidenced by the appearance of SFs [30,31]. Alternatively, the cross-slip usually occurred in metals with high SFE, such as pure Ni, Cu, and Al. The planar-slip in the FCC(L1$_2$) phase and the pinning effect from the FCC(L1$_2$)/BCC(B2) phase boundaries enhanced the strain hardening/dislocation accumulation capability and therefore resulted in the high tensile ductility and high ultimate tensile strength of AlCoCrFeNi$_{2.1}$.

3.2.2. *Deformation of BCC(B2) phase*

Fig. 4 shows bright-field TEM images of the tensile tested EHEA specimen from an alternative region. The BCC(B2) phase had a medium density of dislocations after tension deformation and high density of nano-precipitates (Fig. 4c and d) (composition and structure characterized in the following section). The detailed analysis indicated that the dislocations in the B2 phase could be observed at the [001] zone axis and were mostly located in two slip bands, as displayed more clearly in Fig. 5a. These dislocations were identified in $(\bar{1}\ 10)$ and (110) slip bands, whose two specific directions intersected at 90° [32]. This result was different from the observation in a B2-ordered $Al_{28}Co_{20}Cr_{11}Fe_{15}Ni_{26}$ alloy where two {112} slip bands intersected at 30° [33]. Both bands contained straight and approximately parallel dislocations, which staggered on each other. Nevertheless, these dislocations did not tangle to form a network. Moreover, these dislocations were pinned by the nano-precipitates by leaving a region (marked with a white ellipse) lacking dislocations. Besides parallel dislocation lines, arrow-shaped (marked by white arrows) dislocations in B2 phases were also found (Fig. 5b). The arrow-shaped dislocations were formed in the following manner: when two straight parallel dislocations were

Table 1
Compositions of FCC($L1_2$) and B2 phases as well as nano-precipitates analyzed by APT.

Phase	Al	Co	Cr	Fe	Ni
FCC($L1_2$)	6.43 ± 0.02	21.14 ± 0.02	24.36 ± 0.02	24.16 ± 0.02	23.93 ± 0.02
BCC(B2)	38.56 ± 0.01	10.12 ± 0.01	4.12 ± 0.01	9.20 ± 0.01	37.98 ± 0.01
Precipitates	6.0 ± 0.3	3.4 ± 0.4	79.1 ± 0.3	9.2 ± 0.4	2.4 ± 0.2

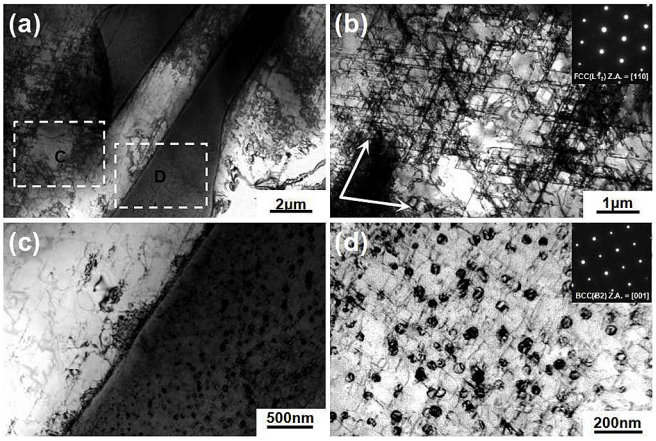

Fig. 4. Bright-field TEM image of the tensile tested EHEA specimen from an alternative region: (a) TEM image with low magnification; (b) magnified TEM image of region "C" in (a) showing two intersected {111} slip traces with zone axis of [110], the inset is the SAED corresponding to the $L1_2$ phase; (c) and (d) magnified images of region "D" in (a) showing nano-precipitates in BCC(B2) phase with zone axis of [001], the inset is the SAED corresponding to the B2 phase.

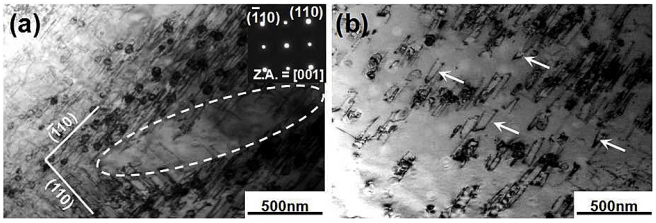

Fig. 5. Bright-field TEM images of the deformed BCC(B2) phase: (a) TEM image showing two crossed slip bands at [001] zone axis, the inset is the SAED corresponding to the B2 phase; (b) TEM image showing arrow-shaped dislocations.

pinned by a nano-precipitate on the tip, the contraction acquired an arrow shape. This result indicated that the precipitate-strengthening effect played an important role in the high strength of B2 phase.

Briefly, the FCC($L1_2$) phase deformed via dislocation planar slip and SFs to act as a soft phase, whereas the B2 phase acted as a hard phase reinforced by nano-precipitates. The modulated hard and soft fine, regular eutectic lamellar structures of $AlCoCrFeNi_{2.1}$ EHEA created the excellent combination of high strength and high ductility.

3.3. Nano-precipitates by APT characterization

The tip specimen was cut by FIB and analyzed by APT analysis to discover the composition of nano-precipitates in the B2 matrix phase. The 3-D atom maps are shown in Fig. 6a. The tip specimen contained a clear phase boundary with both sides containing different elemental distributions (marked with black arrows). Compositions of FCC(L12) and B2 phases are given in Table 1. The FCC(L12) phase comprised Co, Cr, and Fe elements, while the B2 phase comprised Al and Ni elements. Moreover, Fig. 6a also reveals substantial spherical nano-precipitates enriching Cr atoms with sizes less than 20 nm in the B2 phase. Fig. 6b further shows a size distribution of Cr-enriched nano-precipitates. The proportion of Cr-enriched nano-precipitates with sizes less than 5 nm was more than 60% and that of nano-precipitates with sizes bigger than 10 nm was 11% (Fig. 6c).

The quantitative composition analyses of nano-precipitates and BCC as well as FCC phases were further conducted. Fig. 7a is the 1-D proxigram of nano-precipitates showing elemental concentration profiles along the radial direction of their iso-surfaces. The position at $X = 0$ was the interface (defined by the isosurface) of nano-precipitates and B2 matrix, whereas the positions at $X > 0$ and $X < 0$ were nano-precipitate interiors and B2 matrix, respectively. The Y values were average concentration values of all measured nano-precipitates in the B2 phase. Only the Cr concentration curve was seen to rise dramatically from ~3 at.% to ~80 at.% from matrix to nano-precipitate interiors, whereas the other elements (Al, Co, Fe, and Ni) tended to decrease: Al atoms reduced from ~34 at.% to ~6 at.%, Co atoms from ~13 at.% to ~3 at.%, Fe atoms from ~10 at.% to ~8 at.%, and Ni atoms from ~40 at.% to ~2 at.%. The aforementioned result indicated that the nano-precipitate was composed of dominant Cr with minor other elements. Fig. 7b shows 1-D concentration profiles of BCC and FCC phase regions. The concentration variations of all elements were sharp at the phase boundary. Fig. 8 further shows a 3-D atom map (a) and corresponding 1-D concentration profile (b) for a specific nano-precipitate. The nano-precipitate was deficient in Al, Co, and Ni elements but rich in Fe and Cr. The Fe element concentration rose from ~8 at.% to ~12 at.% (at the analyzed position of ~−0.5 nm) and then reduced to ~7 at.% when the analyzed position changed from 0 to 4 nm. Cr element reached the highest value of ~80 at.% at the analyzed position of ~1 nm. The Fe enrichment zone indicated the existence of a thin compositional layer surrounding the Cr-enriched nano-precipitates. The presence of BCC nano-precipitates inside the B2 phase was observed in the $Al_{0.7}CoCrFeNi$ [34] and AlCoCrCuFeNi [35] HEAs, which originated from the spinodal decomposition of compositional modulation [22]. However, the Cr-enriched nano-precipitates with the special structure inside the B2 phase were first detected in the $AlCoCrFeNi_{2.1}$ EHEAs.

3.4. SFs and phase boundary by HRTEM characterization

The qualitative characterization of SFs and atomic structures of eutectic dual phases was performed by HRTEM. Fig. 9a is an HRTEM micrograph showing three SFs in the FCC($L1_2$) phase at [110] zone axis, and Fig. 9b shows a magnified HRTEM image. The inset shows corresponding fast Fourier transformation patterns where weak contrast at the positions of $L1_2$ order diffraction could be seen. The SFs were typical $(\bar{1}\ 11)$ systems in the FCC phase formed by mobile $1/6\langle\bar{1}\ 12\rangle$ Shockley partials. Moreover, two intersected $(\bar{1}\ 11)$ and $(1\bar{1}\ 1)$ SFs were observed in the other regions of FCC($L1_2$) phase, as shown in Fig. 9c. These results indicated that the SF was another important deformation mode besides planar-slip aforementioned in the FCC($L1_2$) phase.

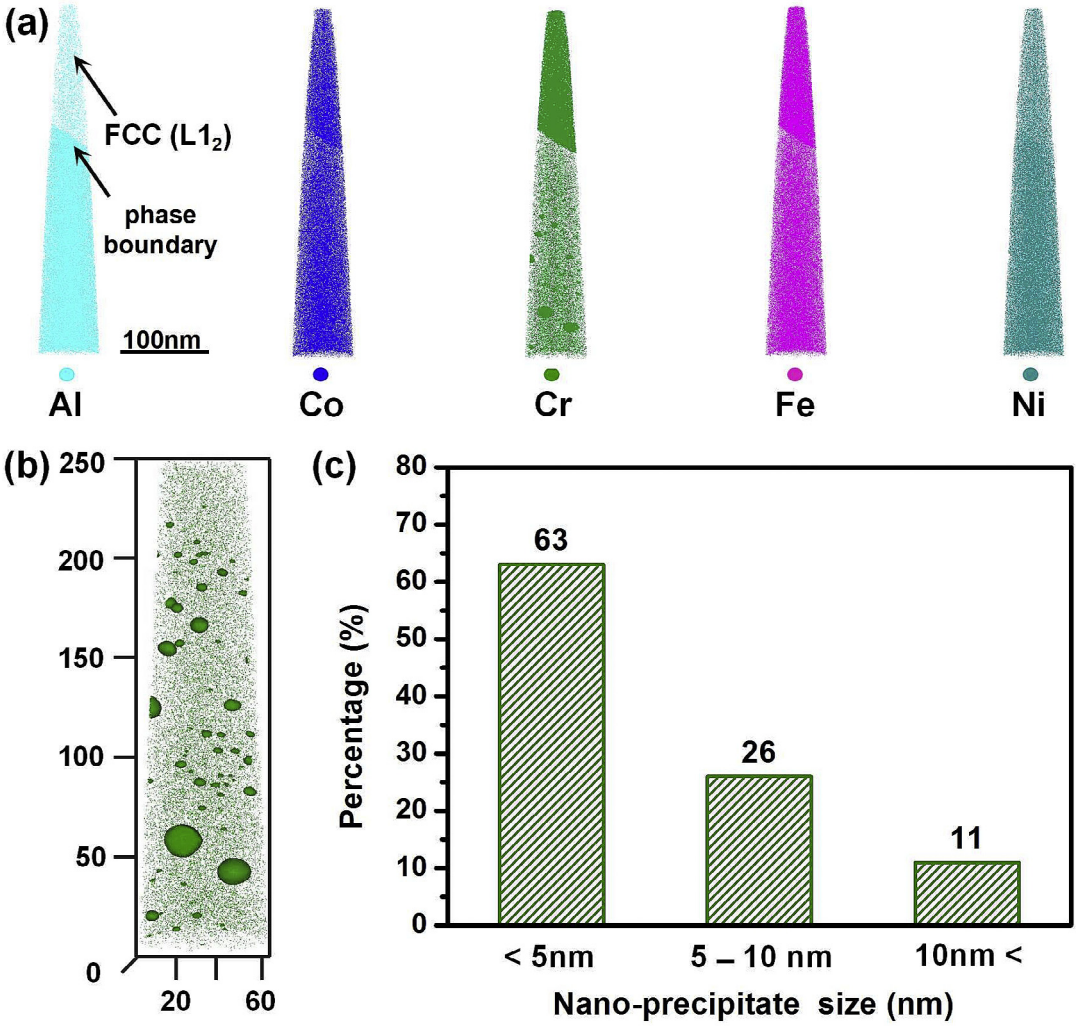

Fig. 6. (a) 3-D atom maps of a tip specimen containing FCC($L1_2$) and BCC(B2) phase boundary of the $AlCoCrFeNi_{2.1}$ alloy. 60% Cr iso-concentration surface shows the outline of Cr-enriched nano-precipitates; (b) 3-D atom maps of BCC(B2) phase containing substantial nano-precipitates, the unit is nm; (c) size distribution of Cr-enriched nano-precipitates.

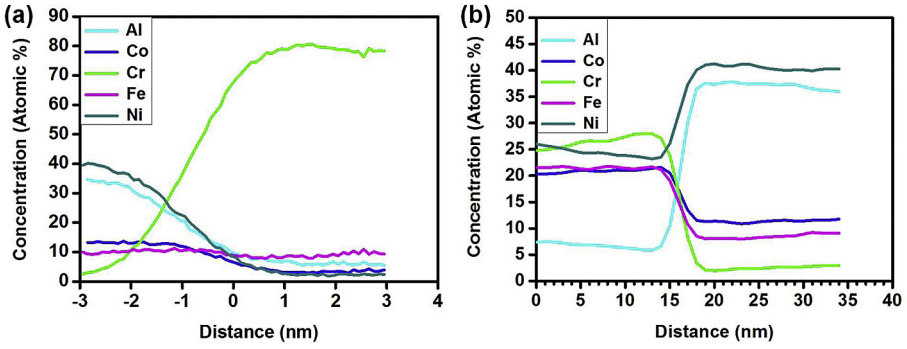

Fig. 7. (a) 1-D concentration profiles of Cr-enriched nano-precipitates; (b) 1-D concentration profiles of the phase boundary.

HRTEM also uncovered the semi-coherent phase boundary between FCC($L1_2$) and BCC(B2) phases (Fig. 9c). Therefore, the combination of eutectic dual phases was at the atomic level and strong enough to bear high stress. The $AlCoCrFeNi_{2.1}$ EHEA with a semi-coherent interface might possess the important value of engineering application in fields of high-temperature creep resistance and high elastic strain energy. Finally, HRTEM was used to uncover the structure of Cr-enriched nano-precipitates (Fig. 9d). A nano-precipitate of about 20 nm in diameter was marked in white spots with the zone axis of [110]. The $(1\bar{1}0)$ and (002) planes of BCC matrix were seen to be perfectly coherent with the nano-precipitate.

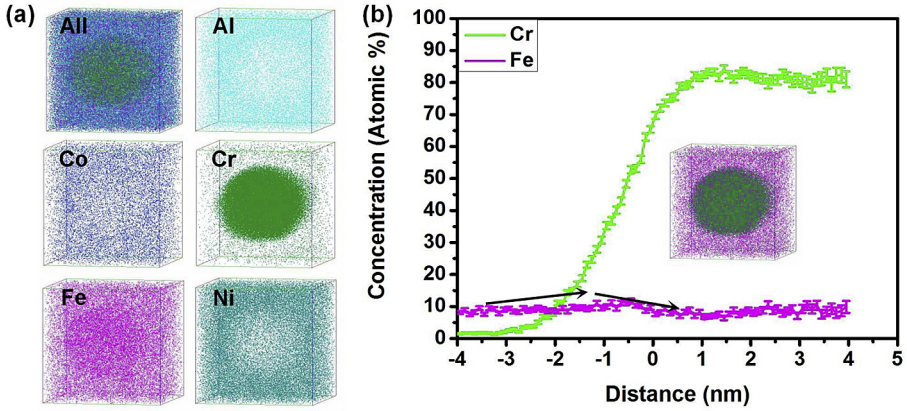

Fig. 8. (a) 3-D atom maps and (b) corresponding 1-D concentration profiles of a specific Cr-enriched nano-precipitate.

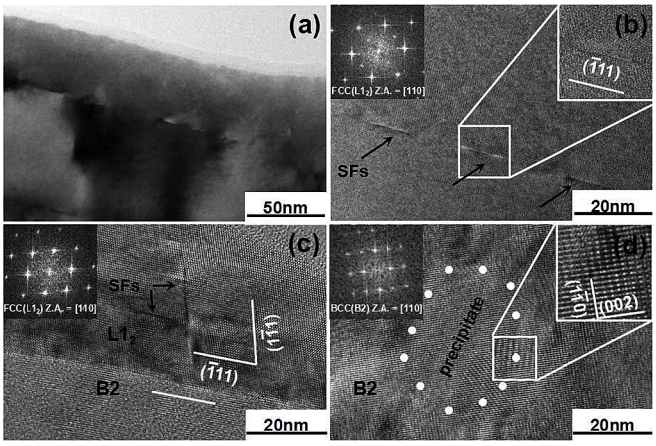

Fig. 9. HRTEM characterization of $AlCoCrFeNi_{2.1}$ alloy: (a) image containing three SFs in FCC($L1_2$) phase; (b) magnified image of the SFs; (c) HRTEM image of the phase boundary and intersected SFs; (d) HRTEM image of a nano-precipitate in BCC(B2) phase. Fourier transformation patterns are insets.

3.5. Fracture mechanisms

SEM observations were performed on the fracture surfaces to further understand the mechanical property and microstructure relationship as well as fracture mechanisms of dual-phase EHEA(-Fig. 10). One could clearly distinguish two different kinds of fracture modes: ductile fracture in the FCC($L1_2$) phase and brittle-like fracture in the BCC(B2) phase. Because the BCC(B2) phase had 3-D spatial structures, several different fracture modes with different crack nucleation and propagations were found and these were determined based on the orientation relationship between the BCC(B2) phase and the stress. In the first fracture mode of BCC(B2) phase (Fig. 10a), the crack was nucleated at the one end of BCC(B2) phase and then propagated through the lamella to the other end by leaving fishbone-shaped crack markings with radial stripes (marked with red solid lines) in the BCC(B2) lamella. However, the FCC($L1_2$) lamellae between the BCC(B2) cracks exhibited a perfect plastic deformation by necking into sharp lines (bright lines) without any dimples. The radial directions of stripes in the BCC(B2) phase were along the crack growth orientation, and the negative directions pointed to the crack sources (marked with red triangles). All crack sources lay on short phase boundaries on the minor axis rather than long phase boundaries on the major axis because stresses gathered on the minor axis easily.

Fig. 10b shows another fracture mode of BCC(B2) phase where cracks were nucleated at the BCC(B2) and FCC($L1_2$) phase boundaries and then propagated along an orientation of 45° related to the phase boundaries. It is clear that massive ~45° shear traces lay on each BCC(B2) phase lamella (as pointed by blue arrows) and evident cracks lay at the phase boundaries. Moreover, the BCC(B2) phase lamellae were broken into several parts by the ~45° cracks (pointed by white arrows). Some cast shrinkage cavities (marked with red arrows) were also observed beside the cracks. These results indicated that stress gathered on the phase boundaries due to dislocation pile-up and induced micro-cracks around the cast shrinkage cavities. The propagation of micro-cracks along the ~45° shear stress in the brittle BCC(B2) phase caused the early shearing fracture, leaving massive shear traces. Finally, the micro-cracks propagated along the phase boundaries, and the FCC($L1_2$) phase fractured the latter by almost a pure shear mode.

The aforementioned findings revealed that the crack first nucleated at the FCC($L1_2$) and BCC(B2) phase boundaries due to stress concentration and then propagated in either normal or shear mode through the BCC(B2) phase, resulting in the fracture of BCC(B2) phase. The load was then imposed to the FCC($L1_2$) phase, and due to the large strain hardening capability, the FCC($L1_2$) phase was subjected to a perfect plastic deformation by necking into sharp lines (bright lines) without any dimples.

4. Discussion

Compared with the traditional metal materials, HEAs possess a specific atomic structure, which is the result of the mixing of elements with different atomic sizes, hence producing deformed lattices. The massive different atoms improve the solid solution strengthening and change the SFE. On the contrary, the frictional stress is assumed to be high due to the large lattice distortion caused by different atomic radii and moduli [19]. Therefore, the significant lattice distortion results in the high ductility and strain hardening of FCC HEAs in the absence of intermetallic phases. The lattice distortion might produce specific deformations of HEAs, which further determine their specific mechanical properties. Careful inspection of the literature, however, indicates that analyses of the deformation mechanisms of such complex alloys and especially the nature of defects are limited [9,11,30,38–40].

The early study on the deformation mechanisms of FCC FeCrNiCoMn using TEM indicated that at a large range of temperatures (77–873 K), plastic deformation occurred by a planar dislocation glide on the classical FCC slip system, {111}<110> and SFs formed through dissociation of the unit dislocation $\boldsymbol{b} = a/2<110>$ in {111}

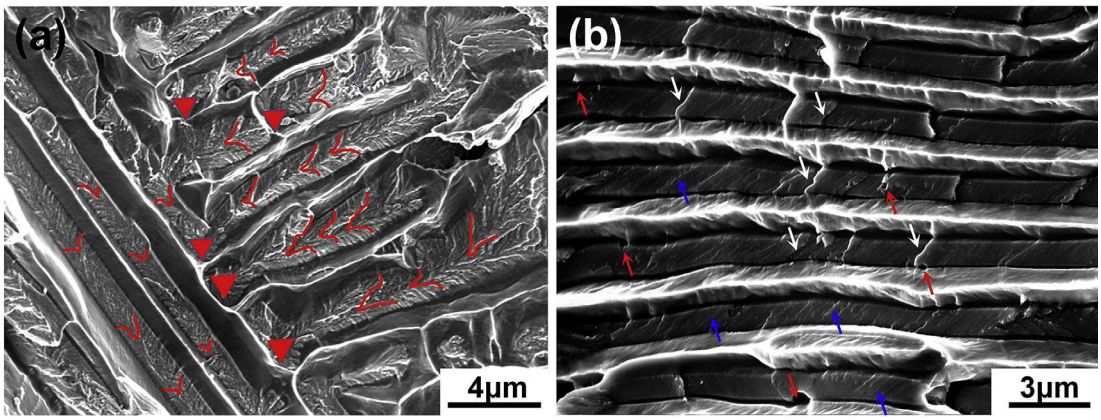

Fig. 10. SEM images showing different fracture modes of the BCC(B2) phase in $AlCoCrFeNi_{2.1}$ alloy. (a) shows the crack was nucleated at one end of the BCC(B2) phase and then propagated through the BCC(B2) to the other end by leaving fish-bone shaped crack markings with radial stripes (marked with red solid lines) in the BCC(B2) lamella. (b) shows cracks were nucleated at the BCC(B2) and FCC($L1_2$) phase boundaries and then propagated along an orientation of 45° related to the phase boundaries. (For interpretation of the references to colour in this figure legend, the reader is referred to the web version of this article.)

plane into 1/6<112> Shockley partials [30]. When the plastic strain was larger than 20%, dislocations re-organized into cell structure, with the size range of 200–300 nm similar to other FCC alloys with low-to-medium SFE, at room temperature, and deformation twinning appeared at 77 K. The authors also suggested that the planar glide might be caused by the low SFE of the alloy or a short-range order effect. The planar dislocation glide was frequently reported in low SFE binary alloys, such as Cu-Al [36] and Cu-Zn [37]. A more recent study of the same FCC FeCrNiCoMn by means of *in situ* TEM observation revealed some unique deformation mechanisms. The planar slip was not continuous with extremely low velocity, which formed close-packed dislocation arrays and pile-ups in the activated {111} due to the strong drag effect of solute atoms [9]. In the present FCC($L1_2$) phase of $AlCoCrFeNi_{2.1}$ EHEA, the observed planar dislocation slip and SFs were consistent with the initial deformation mechanisms of CoCrFeMnNi HEA reported in the literature. However, the planar slip continued to be the only deformation mechanism until the sample broke in the FCC($L1_2$) phase without mechanical nano-twins, or dislocation cells created by the interaction of dislocations and cross-slip on different slip planes. A possible reason for the planar slip was the splitting of 1/2<110> dislocation into 1/6<112> Shockley partials with SFs in between, which would tend to minimize the cross-slip and confine the slip to the primary {111} plane [30]. Massive SFs indicated the extremely low SFE of FCC($L1_2$) phase. Another possible reason might be the low plastic fracture strain (about 18%).

For the BCC HEA, an early study of TiZrHfNbTa HEA indicated that at the meso-scopic level, deformation was not homogeneous but often located in intragranular shear bands [38]. Deformation twins were also observed near grain boundaries. A thermally activated dislocation glide was suggested as the deformation mechanism by the authors based on their analyses of the strain rate and temperature dependences of flow stress [38]. Moreover, the authors also proposed a mechanism based on solid solution strain hardening to explain the deformation behavior of this alloy [11]. More recent investigations of the same BCC TiZrHfNbTa HEA by means of TEM revealed that the dislocation glide was controlled by the movement of screw dislocation at the beginning of deformation, and the deformation was rapidly localized in two distinct bands where dislocation dipoles, loops, and tangles were induced at a higher plastic strain [39,40]. All the observed dislocations identified by the classical extinction rules unambiguously possessed a classical Burgers vector of BCC structure with $\boldsymbol{b} = a/2<111>$. The dislocation patterns observed in the present BCC(B2) phase agreed with the literature results.

Bulk coarse-grained B2 NiAl single-phase alloys are brittle at room temperature. This is because coarse-grained NiAl alloys possess only three independent slip systems that cannot produce cooperative deformation among grains [41]. One could speculate that the B2 rich-NiAl phase in the $AlCoCrFeNi_{2.1}$ EHEA with solid solution strengthening and Cr-enriched precipitate strengthening might be even more difficult to be plastically deformed. However, the results of the present study indicated no cracks at the phase boundary of the tensile deformed specimens (Figs. 3, 4 and 9), which suggested that both the FCC($L1_2$) and BCC(B2) phases were deformed synchronously to about 18% elongation. The observed medium density of dislocations also provided enough evidence for the plastic deformation of BCC(B2) phase. The possible reasons for the enhanced plasticity of brittle BCC(B2) phase in the EHEA alloys might be the complex 3D back-stress states subjected to the FCC($L1_2$) phase. In the literature, the back stress has been verified to improve the plasticity of nanostructured surface layer when adjacent to a coarse-grained core [42]. The back stress was produced in the heterogeneous systems during deformation and maintained the deformation synchronously. In the $AlCoCrFeNi_{2.1}$ EHEA, the boundaries of hard B2 phase and soft FCC($L1_2$) phase were semi-coherent (see Fig. 9c), and these were enveloped by the soft FCC($L1_2$) phase. These conditions favored the occurrence of back-stress effect that could result in massive dislocation in the FCC($L1_2$) phase accumulated at the phase boundaries and activate more dislocations in the BCC(B2) phase compared with the independent coarse-grained NiAl alloys in the uniaxial stressed state during a tensile test.

5. Conclusions

In this study, the $AlCoCrFeNi_{2.1}$ EHEA was prepared using the casting technique. Tensile testing indicated that the EHEA possessed an excellent combination of high strength and high ductility. The un-deformed and post-deformed $AlCoCrFeNi_{2.1}$ EHEAs were further analyzed by means of XRD, EBSD, SEM, TEM, and APT as well as HRTEM. The main conclusions were as follows:

1. Microstructural analyses revealed that the $AlCoCrFeNi_{2.1}$ EHEA possessed a 3-D regular FCC($L1_2$)/BCC(B2) composite structure, that is, a 2-D fine lamellar FCC($L1_2$)/BCC(B2) modulated microstructures with a semi-coherent interface. A high density of Cr-enriched coherent nano-precipitates existed in the B2 phase.
2. Post-deformation analyses revealed a planar slip with

characteristics of high density of parallel dislocation arrays and dense long straight {111} slip traces as well as massive SFs in the FCC($L1_2$) phase, contributing to the high strain hardening and ductility of $AlCoCrFeNi_{2.1}$ EHEA. Moreover, a high density of dislocations pinned by the Cr-enriched nano-precipitates lying on the two {110} slip bands was found in the BCC(B2) phase, contributing to the high strength. In addition, solid solution hardening and semi-coherent phase boundaries also contributed to the high strength by pinning massive dislocations.

3. Fracture surface observations found a ductile fracture in the FCC($L1_2$) phase and a brittle-like fracture in the BCC(B2) lamella. Several fracture modes, including fishbone-shaped crack markings with radial stripes and ~45° shear fracture, were found in the BCC(B2) lamella, and a perfect plastic deformation by necking into one sharp line was found in the FCC($L1_2$) lamella. During tension, cracks first nucleated on the phase boundaries by stress concentration and cast shrinkage cavities and then propagated in the BCC(B2) phase resulting in the fracture of BCC(B2) phase, and the FCC($L1_2$) phase fractured finally with the load further increased.

4. The high strength and high ductility of $AlCoCrFeNi_{2.1}$ EHEA originated from the back stress due to the coupling between the ductile FCC($L1_2$) and brittle BCC(B2) phases during tensile deformation.

Acknowledgements

The authors would like to acknowledge support by Program for New Century Excellent Talents in University from Chinese Ministry of Education, National Natural Science Foundation of China (51225102 and 2012CB932203), The 8th"Liu Da Ren Cai Gao Feng B932203) from Jiangsu Province, China, the Jiangsu Key Laboratory of Advanced Nanomaterials and Technologies.

References

[1] J.W. Yeh, S.K. Chen, S.J. Lin, J.Y. Gan, T.S. Chin, T.T. Shun, C.H. Tsau, S.Y. Chang, Nanostructured high-entropy alloys with multiple principal elements: novel alloy design concepts and outcomes, Adv. Eng. Mater 6 (2004) 299–303.
[2] B. Cantor, I.T.H. Chang, P. Knight, A.J.B. Vincent, Microstructural development in equiatomic multicomponent alloys, Mater. Sci. Eng. A 375–377 (2004) 213–218.
[3] Y. Zhang, T.T. Zuo, Z. Tang, M.C. Gao, K.A. Dahmen, P.K. Liaw, Z.P. Lu, Microstructures and properties of high-entropy alloys, Prog. Mater. Sci. 61 (2014) 1–93.
[4] D.B. Miracle, O.N. Senkow, A critical review of high entropy alloys and related concepts, Acta Mater 122 (2017) 448–511.
[5] Z.P. Lu, H. Wang, M.W. Chen, I. Baker, J.W. Yeh, C.T. Liu, T.G. Nieh, An assessment on the future development of high-entropy alloys: summary from a recent workshop, Intermetallics 66 (2015) 67–76.
[6] Z. Li, K.G. Pradeep, Y. Deng, D. Raabe, C.C. Tasan, Metastable high-entropy dual-phase alloys overcome the strength-ductility trade-off, Nature 534 (2016) 227–230.
[7] B. Gludovatz, A. Hohenwarter, D. Catoor, E.H. Chang, E.P. George, R.O. Ritchie, A fracture-resistant high-entropy alloy for cryogenic applications, Science 345 (2014) 1153–1158.
[8] B. Gludovatz, A. Hohenwarter, K.V.S. Thurston, H. Bei, Z. Wu, E.P. George, R.O. Ritchie, Exceptional damage-tolerance of a medium-entropy alloy CrCoNi at cryogenic temperatures, Nat. Commun. 7 (2016) 10602.
[9] Z. Zhang, M.M. Mao, J. Wang, B. Gludovatz, Z. Zhang, S.X. Mao, et al., Nanoscale origins of the damage tolerance of the high-entropy alloy CrMnFeCoNi, Nat. Commun. 6 (2015) 10143.
[10] Y. Zou, H. Ma, R. Spolenak, Ultrastrong ductile and stable high-entropy alloys at small scales, Nat. Commun. 6 (2015) 7748.
[11] O.N. Senkov, J.M. Scott, S.V. Senkova, F. Meisenkothen, D.B. Miracle, C.F. Woodward, Microstructure and elevated temperature properties of a refractory TaNbHfZrTi alloy, J. Mater. Sci. 47 (2012) 4062–4074.
[12] L.J. Santodonato, Y. Zhang, M. Feygenson, C.M. Parish, M.C. Gao, R.J.K. Weber, J.C. Neuefeind, Z. Tang, P.K. Liaw, Deviation from high-entropy configurations in the atomic distributions of a multi-principal-element alloy, Nat. Commun. 6 (2015) 5964.
[13] P. Koželj, S. Vrtnik, A. Jelen, S. Jazbec, Z. Jagličić, S. Maiti, M. Feuerbacher, W. Steurer, J. Dolinšek, Discovery of a superconducting high-entropy alloy, Phys. Rev. Lett. 113 (10) (2014) 107001.
[14] C. Jiang, B.P. Uberuaga, Efficient Ab initio modeling of random multicomponent alloys, Phys. Rev. Lett. 116 (10) (2016) 105501.
[15] O.N. Senkov, J.D. Miller, D.B. Miracle, C. Woodward, Accelerated exploration of multi-principal element alloys with solid solution phases, Nat. Commun. 6 (2015) 6529.
[16] J.Y. He, H. Wang, H.L. Huang, X.D. Xu, M.W. Chen, Y. Wu, X.J. Liu, T.G. Nieh, K. An, Z.P. Lu, A precipitation-hardened high-entropy alloy with outstanding tensile properties, Acta Mater 102 (2016) 187–196.
[17] Y. Deng, C.C. Tasan, K.G. Pradeep, H. Springer, A. Kostka, D. Raabe, Design of a twinning-induced plasticity high entropy alloy, Acta Mater 94 (2015) 124–133.
[18] M.J. Yao, K.G. Pradeep, C.C. Tasan, D. Raabe, A novel single phase non-equiatomic FeMnNiCoCr high-entropy alloy with exceptional phase stability and tensile ductility, Scr. Mater. 72–73 (2014) 5–8.
[19] Y. Zou, S. Maiti, W. Steurer, R. Spolenak, Size-dependent plasticity in an $Nb_{25}Mo_{25}Ta_{25}W_{25}$ refractory high-entropy alloy, Acta Mater 65 (2014) 85–97.
[20] Y. Lu, Y. Dong, S. Guo, L. Jiang, H. Kang, T. Wang, B. Wen, Z. Wang, J. Jie, Z. Cao, H. Ruan, T. Li, A promising new class of high-temperature alloys: eutectic high-entropy alloys, Sci. Rep. 4 (2014) 6200.
[21] I.S. Wani, T. Bhattacharjee, S. Sheikh, Y.P. Lu, S. Chatterjee, P.P. Bhattacharjee, S. Guo, N. Tsuji, Ultrafine-grained $AlCoCrFeNi_{2.1}$ eutectic high-entropy alloy, Mater. Res. Lett. (2016) 1–6.
[22] I.S. Wani, T. Bhattacharjee, S. Sheikh, P.P. Bhattacharjee, S. Guo, N. Tsuji, Tailoring nanostructures and mechanical properties of $AlCoCrFeNi_{2.1}$ eutectic high entropy alloy using thermo-mechanical processing, Mater. Sci. Eng. A 675 (2016) 99–109.
[23] T. Yang, S. Xia, S. Liu, C. Wang, S. Liu, Y. Zhang, J. Xue, S. Yan, Y. Wang, Effects of Al addition on microstructure and mechanical properties of AlxCoCrFeNi High-entropy, Mater. Sci. Eng. A 648 (2015) 15–22.
[24] C. Li, M. Zhao, J.C. Li, Q. Jiang, B2 structure of high-entropy alloys with addition of Al, J. Appl. Phys. 104 (2008) 113504.
[25] J.Y. He, W.H. Liu, H. Wang, Y. Wu, X.J. Liu, T.G. Nieh, Z.P. Lu, Effects of Al addition on structural evolution and tensile properties of the FeCoNiCrMn high-entropy alloy system, Acta Mater 62 (2014) 105–113.
[26] H. Wei, J.J. Liang, B.Z. Sun, P. Peng, Q. Zheng, X.F. Sun, M.S. Dargusch, X. Yao, Comparison of valence-band structures of NiAl alloy containing Cr and Ti: photoelectron spectrum and first-principles calculations, Intermetallics 18 (2010) 1062–1066.
[27] Y. Cao, P.X. Zhu, J.C. Zhu, Y. Liu, First-principles study of NiAl alloyed with Co, Comput. Mater. Sci. 111 (2016) 34–40.
[28] J.M. Zhang, D.D. Wang, G.X. Chen, K.W. Xu, Surface structure and energy of B2 type intermetallic compound NiAl, Appl. Surf. Sci. 254 (2008) 2540–2543.
[29] A.K. Head, P. Hunble, L.K. Clarebrough, A.J. Morton, C.T. Forwood, Computed Electron Micrographs and Defect Identification, North-Holland Pub. Company, Amsterdam, 1973, pp. 60–69.
[30] F. Otto, A. Dlouhý, Ch. Somsen, H. Bei, G. Eggeler, E.P. George, The influence of temperature and microstructure on the tensile properties of a CoCrFeMnNi high-entropy alloy, Acta Mater 61 (2013) 5743–5755.
[31] G. Laplanche, A. Kostka, O.M. Horst, G. Eggeler, E.P. George, Microstructure evolution and critical stress for twinning in the CrMnFeCoNi high-entropy alloy, Acta Mater 118 (2016) 152–163.
[32] Y.Q. Sun, N. Yang, The onset and blocking of <011> slip in NiAl, Acta Mater 51 (2003) 5601–5612.
[33] M. Feuerbacher, Dislocation and deformation microstructure in a B2-ordered $Al_{28}Co_{20}Cr_{11}Fe_{15}Ni_{26}$ high-entropy alloy, Sci. Rep. 6 (2016) 29700.
[34] A.M. Giwa, P.K. Liaw, K.A. Dahmen, J.R. Greer, Microstructure and small-scale size effects in plasticity of individual phases of $Al_{0.7}$CoCrFeNi high entropy alloy, Extrem. Mech. Lett. 8 (2016) 220–228.
[35] C.C. Tung, J.W. Yeh, T.T. Shun, S.K. Chen, Y.S. Huang, H.C. Chen, On the elemental effect of AlCoCrCuFeNi high-entropy alloys system, Mater. Lett. 61 (2007) 1–5.
[36] R. Liu, Z.J. Zhang, L.L. Li, X.H. An, Z.F. Zhang, Microscopic mechanisms contributing to the synchronous improvement of strength and plasticity (SISP) for TWIP copper alloys, Sci. Rep. 5 (2015) 9550.
[37] Y.H. Zhao, Y.T. Zhu, X.Z. Liao, Z. Horita, T.G. Langdon, Tailoring stacking fault energy for high ductility and high strength in ultrafine grained Cu and its alloy, Appl. Phys. Lett. 89 (2006) 121906.
[38] O.N. Senkov, J.M. Scott, S.V. Senkova, D.B. Miracle, C.F. Woodward, Microstructure and room temperature properties of a high-entropy TaNbHfZrTi alloy, J. Alloy. Compd. 509 (2011) 6043–6048.
[39] J.Ph. Couzinié, L. Lilensten, Y. Champion, G. Dirras, L. Perrière, I. Guillot, On the room temperature deformation mechanisms of a TiZrHfNbTa refractory high-entropy alloy, Mater. Sci. Eng. A 645 (2015) 255–263.
[40] G. Dirras, L. Lilensten, P. Djemia, M. Laurent-Brocq, D. Tingaud, J.-P. Couzinié, L. Perrière, T. Chauveau, I. Guillot, Elastic and plastic properties of as-cast equimolar TiHfZrTaNb high-entropy alloy, Mater. Sci. Eng. A 654 (2016) 30–38.
[41] R.D. Nobe, R.R. Bowan, et al., Physics and mechanical properties of the B2 compound NiAl, Int. Mater. Rev. 38 (1993) 193–201.
[42] X. Wu, M. Yang, F. Yuan, G. Wu, Y. Wei, X. Huang, Y. Zhu, Heterogeneous lamella structure unites ultrafine-grain strength with coarse-grain ductility, PNAS 112 (2015) 14501–14505.